



Anchoring atomically dispersed FeN₅ sites on porous and defect-rich biochar via cascade regulation strategy for efficient Fenton-like catalysis

Qing Du, Changqing Zhu, Cailiang Yue, Fenxian Cun, Zhiling Du, Fuqiang Liu^{*}, Aimin Li

State Key Laboratory of Pollution Control and Resource Reuse, School of the Environment, Nanjing University, Nanjing 210023, PR China

ARTICLE INFO

Keywords:

Biochar
Cascade regulation
Atomically dispersed FeN₅ sites
Fenton-like catalysis
Peroxymonosulfate activation

ABSTRACT

Biochar-based single-atom catalyst with atomically dispersed FeN₅ sites (Fe-N-FPBC) is rationally prepared through a micropores construction-functionalization-N doping cascade regulation strategy. The as-synthesized Fe-N-FPBC is rich in micropores and defects which are crucial for effective N doping to achieve FeN₅ sites. The electron transfer mediated by Fe-N-FPBC contributes to the ultra-fast degradation of sulfamethoxazole via peroxymonosulfate activation. The catalyst-dosage-normalized kinetic constant is 52.63 L min⁻¹ g⁻¹, out-distancing reported values. Density-Functional-Theory calculations reveal that the FeN₅ site exhibits favorable global energy compared to FeN₄ site. The axial ligand of FeN₅ site results in thermodynamically facilitated electron extraction from contaminants, and also leads to the easier desorption of -SO₄H for rapid site regeneration. Overall, this work provides a pathway for the fabrication of biochar-based single-atom catalyst with high metal-N coordination number for efficient Fenton-like catalysis.

1. Introduction

With rapid economic and industrial development, the pollution of water environment by organic pollutants poses a great threat to human health and ecological safety [1–3]. Therefore, it is crucial to develop efficient and economical water purification technologies. Among these, advanced oxidation processes (AOPs) that aim for the complete degradation of various toxic organic pollutants is an essential choice [4]. Currently, nanomaterial-based activation of peroxymonosulfate (PMS) technology is an important technique for organic wastewater control due to its advantages of high oxidation capacity, wide pH adaptation range, and controllable pathways [5,6]. However, representative nanoscale metal oxide-based catalysts suffered from low metal atom utilization and severe metal leakage during the PMS activation process, which significantly restricted the practical application of PMS-based Fenton-like AOPs [7]. Furthermore, nanocarbon-based catalysts have garnered attention due to their advantages like zero metal leakage and low preparation costs [8]. However, nanocarbon-based catalysts still faced challenges, including a limited number of active sites and lower reaction efficiency, which prevented them from meeting practical application requirements.

The activation of PMS using single-atom catalysts (SACs) with metal-nitrogen-carbon (M-N-C) sites is a recent research hotspot [7,9]. SACs

can not only avoid metal leakage through strong coordination, but also exhibit high PMS-based Fenton-like efficiency due to the unsaturated metal coordination structure and maximized atom utilization [6,10]. Currently, to obtain higher adsorption energy for PMS, the N coordination number of metal sites is deliberately lowered by modulating the synthesis condition like increasing the pyrolysis temperature [11]. However, the metal sites with low coordination number also has strong adsorption strength to PMS-derived product molecules, leading to difficulties in product desorption and site regeneration, which will limit the further improvement of SACs' efficiency [12]. Single-atom metal sites with high N coordination number (Metal-N_x, x > 4) have recently received attention in the field of energy conversion and fine synthesis [13,14]. The single-atom metal sites retain the unsaturated coordination structure, allowing them to still adsorb and activate PMS, while the energy barrier for product molecules to desorb from the sites is reduced due to its high coordination saturation [12]. The overall moderate adsorption strength to adsorbates contributes to the rapid and recyclable operation of the sites, ultimately leading to efficient catalysis. Specifically, Zhang et al. found that the low electron density and suitable adsorption strength of FeN₅ site achieved efficient CO₂ electrocatalytic reduction due to the low-energy-barrier desorption of the CO product [14]. However, there is still a lack of details on how to construct the microenvironment for high-coordinated single-atom metal sites

^{*} Corresponding author.

E-mail address: lfq@nju.edu.cn (F. Liu).

<https://doi.org/10.1016/j.apcatb.2023.123570>

Received 3 August 2023; Received in revised form 25 October 2023; Accepted 25 November 2023

Available online 29 November 2023

0926-3373/© 2023 Elsevier B.V. All rights reserved.

formation, making it difficult to synthesize this type of SACs rationally.

Biomass is widely available, inexpensive, and proved to be a sustainable precursor for the preparation of carbon support to anchor metal atoms [15,16]. Yin et al. used marine Fe-rich marsh moss as the precursor to prepare Fe single-atom catalyst, but the coordination structure of Fe species was FeN_4 [17]. It is well-established that pyrolyzing the mixture of carbon material and alkali (e.g. KHCO_3 , KOH) can etch abundant nanopores on the carbon matrix while generating a large number of carbon vacancies (CVs) in the pore wall [18]. When the N-containing gases produced by N precursors (e.g. urea, melamine) enter the defect-rich pores, these CVs can serve as effective sites for N doping at high temperature. More importantly, the nanopores are expected to increase the N doping amount through the diffusion-limited effect, which will increase the N coordination number around metal atoms [18,19]. Therefore, constructing the biochar support with plentiful micropores and CVs could facilitate the preparation of low-cost SACs featuring metal sites with high N coordination number.

Inspired by these, we proposed a cascade control strategy of micropores construction-functionalisation-N doping to prepare the desired SAC (Fe-N-FPBC) with atomically dispersed FeN_5 sites on porous and defect-rich biochar support. This method could gradually create an optimal micro-environment for Fe species to coordinate with more N atoms, and ultimately, the successful loading of atomically dispersed FeN_5 sites on the biochar support was achieved. Sulfamethoxazole (SMZ) was used as the model contaminant due to its difficulty in biodegradation, and its release into the environment could easily disrupt the functionality of animal gut microbiota and potentially induce malformations [20]. The structure-activity relationship of Fe-N-FPBC was illustrated in detail by systematic characterizations and performance experiments. Pathway of contaminant degradation was revealed by quenching experiments, electron paramagnetic resonance spectroscopy and molecular probes. Subsequently, the reduced toxicity of intermediates from SMZ degradation by the Fe-N-FPBC/PMS system was verified by the Toxicity Estimation Software Tool (T.E.S.T.) prediction and corn seed cultivation toxicity experiments. Finally, electrochemical experiments and Density-Functional-Theory (DFT) calculations were used to explore the mechanism underlying the ultra-fast degradation kinetics and interference resistance of Fe-N-FPBC with FeN_5 sites.

2. Experimental section

2.1. Chemicals

In this study, all the chemical reagents were used analytically pure, and all solutions were prepared by using ultra-pure water (Millipore, 18.25 $\text{M}\Omega\cdot\text{cm}$) for all experiments. Rice husks (RH) were collected from Wuchang City, Heilongjiang Province, China. Potassium peroxomonosulfate ($2\text{KHSO}_5\cdot\text{KHSO}_4\cdot\text{K}_2\text{SO}_4$, as the source of PMS), potassium bicarbonate (KHCO_3), sodium hydroxide (NaOH), hydrogen peroxide (H_2O_2), sodium sulfate (Na_2SO_4), sodium chloride (NaCl), sodium bicarbonate (NaHCO_3), sodium dihydrogen phosphate (NaH_2PO_4), sodium nitrate (NaNO_3), hydrochloric acid (HCl), heavy water (D_2O), phenyl methyl sulfoxide (PMSO), phenyl methyl sulfone (PMSO_2), nitric acid (HNO_3), 5,5-dimethyl-1-pyrroline N-oxide (DMPO), Ferric chloride hexahydrate ($\text{FeCl}_3\cdot 9\text{H}_2\text{O}$) ethanol, L-histidine, potassium thiocyanate (KSCN), tert-butyl alcohol (TBA), potassium iodide (KI), nitro blue tetrazolium chloride monohydrate (NBT), p-benzoquinone (PBQ), methyl orange (MO), bisphenol A (BPA), phenol and sulfamethoxazole (SMZ) were provided by Sinopharm Chemical Reagent Co., Ltd. (China). 2,2,6,6-tetramethyl-4-piperidone (TEMP) were provided by Adams Reagent Co., Ltd.

2.2. Materials preparation

2.2.1. Preparation of functionalized porous biochar (FPBC)

Firstly, rice husks (RH) were washed, dried (105°C), smashed, and

sieved through a 100-mesh sieve to obtain RH powder. The RH powder and KHCO_3 were mixed in a mass ratio of 1:2 and heated to 800°C for 2 h at a heating rate of 5°C min^{-1} under Ar protection. Then the obtained solid product was washed with 2 mol L^{-1} HCl to remove the residual $\text{HCO}_3^-/\text{CO}_3^{2-}/\text{K}_2\text{O}$, and washed with deionized water until neutral and dried under vacuum at 60°C to obtain porous biochar (PBC). Finally, 0.5 g of PBC was added to 50 mL of 5% H_2O_2 and reacted continuously at 60°C for 2 h, then the reaction solid product was washed and vacuum dried at 60°C to obtain the functionalized porous biochar (FPBC). In addition, the biochar (BC) prepared without KHCO_3 and its functional product (FBC) were prepared according to the above methods.

2.2.2. Preparation of Fe-N-FPBC with FeN_5 sites

Firstly, 0.1 g of FPBC was added to 50 mL of Fe^{3+} solutions ($C_{\text{Fe}} = 0, 0.5, 1.0, 2.0$, and 4.0 mmol L^{-1}) and pH was adjusted to 2.5 (reduces the hydrolysis of Fe^{3+}), and then the reaction was stirred continuously at room temperature for 2 h to reach Fe^{3+} adsorption equilibrium. Then, the reacted solid-liquid mixture was repeatedly filtered and washed by deionized water until neutral to remove the weakly bound Fe^{3+} , and vacuum dried at 60°C to obtain the Fe-enriched FPBC (Fe@FPBC). Finally, Fe@FPBC was evenly mixed with 0.4 g of urea (the mass ratio of FPBC to urea was 1:4). The mixture was initially heated from room temperature to 500°C for 1 h and then again heated to 800°C for 2 h at 5°C min^{-1} under Ar protection. Finally, catalyst composites with different Fe contents were prepared, named Fe-N-FPBC-x ($x = 0, 0.5, 1.0, 2.0, 4.0\text{ mmol L}^{-1}$, x as the C_{Fe}). When $x = 1.0$, the target material was named Fe-N-FPBC. Furthermore, following the aforementioned target material preparation method, Fe-N-FBC, Fe-N-PBC, and Fe-FPBC were also synthesized.

2.3. Characterizations

Thermogravimetric analysis (TGA) data were collected with a NETZSCH-STA-449 C thermal balance in N_2 atmosphere with a heating rate of 5°C min^{-1} . X-ray diffraction (XRD) patterns of samples were recorded on a Rigaku RINT 2000 X-ray instrument with monochromatic $\text{Cu K}\alpha$ radiation (40 kV, 40 mA) at a scanning rate of 1° min^{-1} . The morphology and microstructure were characterized on a scanning electron microscope (FEI Quanta 400EFG, SEM) at an accelerating voltage of 5 kV. Transmission electron microscopy (TEM) was operated by JEOL JEM-ARM200F working at 100 kV. High-resolution transmission electron microscopy (HRTEM), selected area electron diffraction (SAED), atomic high-angle annular dark-field scanning transmission electron microscopy (HAADF-STEM) and energy-dispersive X-ray spectroscopy (EDS) elemental mapping were conducted on FEI Talos F200S STEM/TEM with a spherical aberration corrector working at 200 kV. Fourier transform infrared spectra (FT-IR) were collected by the infrared spectrometer (NEXUS 870, America). The chemical environments of samples were measured by X-ray photoelectron spectroscopy (XPS Thermo Scientific K-Alpha). The specific surface area and pore size distribution of the samples were tested with the Brunauer-Emmett-Teller method (Micrometrics ASAP 2460). Raman spectra were recorded on a Thermo Fisher DXR Raman spectrometer employing a 532 nm laser. X-ray absorption fine structure (XAFS) spectra were obtained at the 1W1B station in the BSRF (Beijing Synchrotron Radiation Facility, China) operated at 2.5 GeV with a maximum current of 250 mA. The measurements at the Fe K-edge were performed in fluorescence mode using a Lytle detector. The Zeta potentials of samples were measured by the Malvern Zetasizer 3000 HSA. The inductively coupled plasma optical emissionspectrometry (ICP-OES) measurements were undertaken on Avio 200, PerkinElmer. Electrochemical impedance spectroscopy (EIS), chronoamperometry, and chronopotentiometry were performed on electrochemical workstations (CHI 660E, China) in Text. S1.

2.4. Catalytic degradation procedure

The catalytic performance of the catalysts in the PMS-AOPs was assessed for the removal of organic pollutants. The concentrations of SMZ, the as-prepared Fe-N-FPBC catalyst, and PMS were determined 20 mg L⁻¹, 80 mg L⁻¹ and 75 mg L⁻¹, respectively. Typically, 8 mg catalyst was added into 100 mL of 20 mg L⁻¹ SMZ solution. Ultrasonic dispersion was performed for 20 min to make the dispersion uniform to form a suspension, and then stirred for 10 min to establish adsorption-desorption equilibrium. The adsorption performance of the catalyst for SMZ was tested by membrane rejection and methanol desorption. The detailed calculation methods were shown in **Text. S2**. Subsequently, 0.375 mL 10 g L⁻¹ PMS solution was added to the suspension to initiate the reaction. At set time intervals, 0.5 mL the suspension was taken out and injected into 1.0 mL methanol to terminate the reaction and facilitate the desorption of undegraded SMZ. Afterwards, the samples were filtered through 0.22 µm polytetrafluoroethylene (PTFE) filters into high performance liquid chromatography (HPLC) vials for subsequent SMZ concentration measurements.

2.5. Analytic methods

The concentrations of SMZ were analyzed on a high-performance liquid chromatography (HPLC) system (Agilent 1200 infinity Series) equipped with a multi-wavelength UV detector. A mobile phase consisting of a 0.68% KH₂PO₄ solution (pH adjusted to 3 using H₃PO₄) and acetonitrile in a ratio of 60:40 (v/v) was used. The mobile phase flow rate was set at 1.0 mL min⁻¹. The test wavelength for detection was 270 nm. The detailed calculation methods were shown in **Text. S3**. The concentration of Fe ions released from the material after the reaction was measured using inductively coupled plasma atomic emission spectrometry (ICP 8000, USA). The UV-Vis spectra of NBT solutions were recorded to probe O₂^{•-} by a UNICO spectrometer operating between 190 and 700 nm. The electron paramagnetic resonance (EPR) measurement was conducted using a Bruker ELEXSYS 580 spectrometer to detect ROSS or ¹O₂ during PMS activation using DMPO or TEMP as the spin-trapping agents. Total organic carbon (TOC) was determined with a TOC analyzer (Elementar, Germany). SMZ degradation process intermediates were determined by gas chromatography-mass spectrometer (GC-MS) in **Text. S3**.

2.6. Corn seeds cultivation toxicity experiment

Initially, 90 healthy corn seeds were carefully chosen and subjected to a 20 min immersion in a 5% H₂O₂ solution for disinfection. Subsequently, the seeds were thoroughly rinsed three times with ultra-pure water. From the initial set, 80 seeds were selected and divided into four groups, each consisting of 20 seeds. These seeds were then soaked in equal volumes of deionized water, SO₄²⁻ solution (0.99 mmol L⁻¹), SMZ reaction solution, and SMZ stock solution (20 mg L⁻¹) for a duration of 24 h. The pH values of all solutions were adjusted at about 7. Second, the soaked seeds were individually placed in sterilized petri dishes and immersed in the corresponding solutions mentioned above. The seeds were placed in a constant temperature incubator at 25 °C for continuous cultivation (cultivated under shaded conditions). Furthermore, the growth dynamic process of corn buds were meticulously recorded by capturing photographs and the biomass of corn buds (root and shoot length) was measured. Finally, 8 corn buds with similar growth states were selected and transplanted to a centrifuge tube equipped with corresponding solutions for further light culture. The growth state of corn seedlings was recorded every day, and the biomass (root and stem length) was measured on the 8 th day.

2.7. Computational methods

Spin-polarized density functional theory (DFT) calculations

conducted using by using the Vienna Ab-initio Simulation Package (VASP). The interactions between ions and electrons were described using the PBE function and the PAW method. The energy cutoff for the plane wave was set to be 480 eV. Fe-N-FPBC with Fe-N₅ sites model structure: a periodic slab model represented by four N atoms in a monolayer of pyridine N-doped graphene and a pyrrole N molecule in the axial direction fixing one Fe atom. Contrast construction of FeN₄ model structure: a periodic slab model represented by four N atoms in a single layer of pyridine N-doped graphene fixing one Fe atom. PMS was placed on top of the FeN₅ or FeN₄ sites within the graphene. The unit cell of the slab model had dimensions of approximately 9.79 Å × 12.24 Å × 25 Å, α = β = 90°, γ = 120°. All atoms were allowed to relax during the calculations. The convergence criterion for the total energy was set to 10⁻⁵ eV, while for the force, it was set to 0.02 eV Å⁻¹.

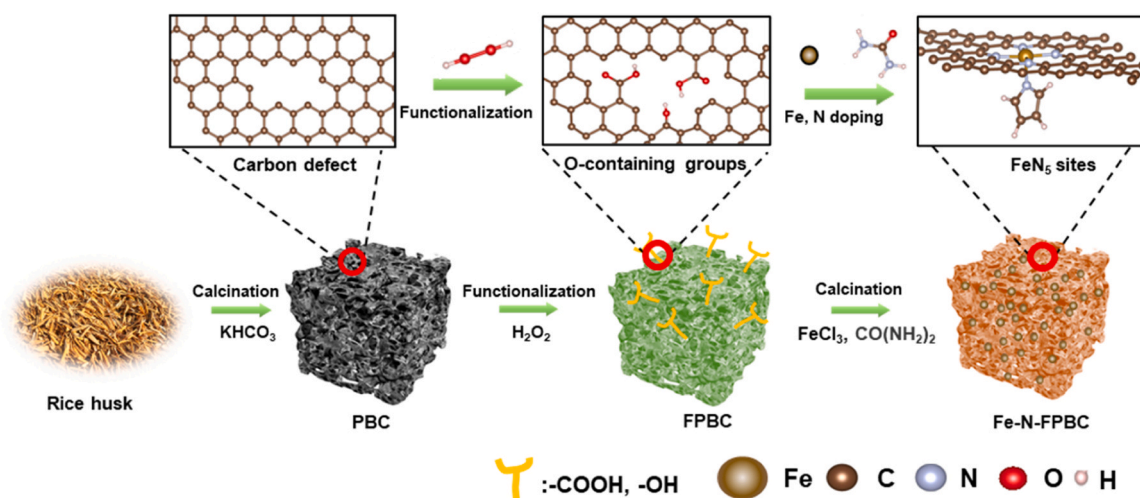
3. Results and discussion

3.1. Synthesis and characterization

The synthesis process of Fe-N-FPBC by cascade regulation strategy was shown in **Scheme 1**. Firstly, KHCO₃ was used as the pore-forming agent to etch rice husks (RH) during pyrolysis for preparing PBC with abundant micropores and CVs. Secondly, H₂O₂ was used as an oxidizing agent to construct more functional groups like 'tentacles' on the surface of PBC to obtain FPBC, increasing the binding sites for Fe³⁺. Finally, the Fe³⁺-anchored FPBC was homogeneously mixed with urea and then pyrolyzed to obtain Fe-N-FPBC with FeN₅ sites.

The scanning electron microscope (SEM) images showed that Fe-N-FPBC (**Fig. 1a**) and PBC (**Fig. S1a**) had similar three-dimensional honeycomb-like porous structure, while BC surface was smooth (**Fig. S1b**). The specific surface area (SSA) of PBC increased from 264.68 m² g⁻¹ of BC to 1023.87 m² g⁻¹, and abundant micropores with the pore size concentrated at 0.67 nm were produced (**Fig. 1b** and **Table S1**). These results demonstrated that a significant number of micropores was created on the surface of PBC by etching with molten salt. What's more, thermogravimetric analysis (TGA) showed a significant mass loss of 72.60% during the molten KHCO₃ etching of the biochar, indicating that a significant amount of gas was released (**Fig. S2** and **Eqs. S4-7**). Meanwhile, in the X-ray diffraction (XRD, **Fig. 1c**) pattern, the peak intensity at 2θ = 26° of PBC, which was assigned to the (002) lattice plane of graphitic carbon, was much lower than that of BC. These results indicated that the generation of large amounts of gas between the graphite carbon layers increased their internal pressure in favour of reducing the thickness of the graphite carbon layers and thus increasing the SSA. In addition, Raman spectroscopy (**Fig. 1d**) showed that the intensity ratio of D band and G band (I_D/I_G) of BC was 0.962, while the I_D/I_G of PBC was 1.034, respectively, indicating that the amount of CVs could be greatly increased by using KHCO₃ etching [21].

Previous studies have shown that high temperature was favorable for biochar to fully carbonize and construct pore structure, but the number of O-containing groups in biochar decreased sharply with increasing pyrolysis temperature, which was unfavorable for biochar to anchor more Fe³⁺ [22,23]. The fourier transform infrared spectroscopy (FT-IR) analysis revealed that the absorption peak intensities of C=O/COOH (~1691 cm⁻¹) and -OH (3430 cm⁻¹) on the surface of FPBC were noticeably higher than those on PBC (**Fig. 1e**), indicating the presence of a higher concentration of polar O-containing functional groups on the FPBC surface [24]. UV dispersibility and static settling experiments (**Fig. 1f**) confirmed that FPBC exhibited better dispersion in water than PBC, possibly attributed to the electrostatic repulsion among the O-containing functional groups on the FPBC surface, which was consistent with the research conclusion reported by Yang et al. [25]. Additionally, the strong signal captured by the solid-state electron paramagnetic resonance (EPR) spectrum at g = 2.003 further confirmed the presence of a large number of CVs on the surface of the PBC, and the signal intensity of CVs of FPBC was lower than PBC (**Fig. 1g**) [21]. These



Scheme 1. Schematic illustration for the synthesis process of porous biochar-based SAC with FeN₅ sites (Fe-N-FPBC).

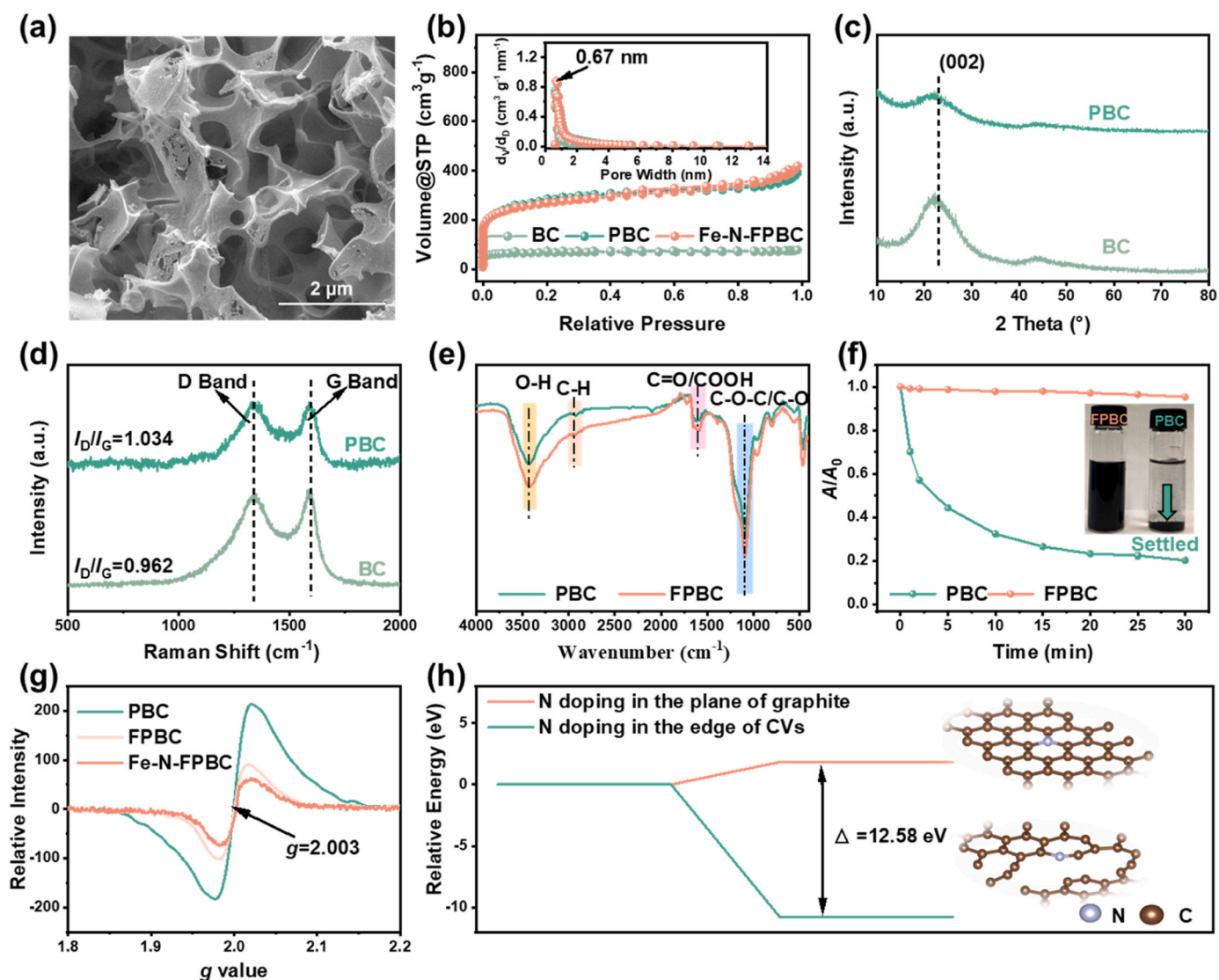


Fig. 1. (a) SEM image of Fe-N-FPBC. (b) N_2 adsorption-desorption isotherms and pore size distributions (inset) of BC, PBC, and Fe-N-FPBC. (c) XRD patterns of BC and PBC. (d) Raman spectra of the BC and PBC. (e) FT-IR spectra of PBC and FPBC. (f) Sedimentation curves of PBC and FPBC dispersed solutions (2.0 g L⁻¹) measured by UV ($\lambda = 500$ nm). (g) Solid EPR spectra of PBC, FPBC, and Fe-N-FPBC. (h) Relative free energy of N-doping in the edge of CVs model and plane of graphite model (inset).

results indicated that more O-containing groups were constructed on FPBC by H_2O_2 through oxidizing the CVs edges of PBC. Thus, these O-containing groups enabled FPBC to bond more Fe^{3+} than PBC (Fe loading: 1.28 wt% of Fe-N-FPBC vs 0.73 wt% of Fe-N-PBC, Table S2). Furthermore, efficient N doping is essential to achieve a high N coordination number of Fe. According to the elemental analysis results (Table S3), PBC with micropores-rich and CVs edges facilitated N doping compared with the unactivated BC (N doping: 0.66 wt% of NBC vs 2.95 wt% of NPBC). After Fe and N doping, the EPR signal of Fe-N-FPBC weakened, indicating that Fe and N atoms were likely incorporated into CVs, neutralizing the unpaired electrons on the surface of FPBC (Fig. 1g).

Additionally, DFT calculations demonstrated that constructing biochar with rich CVs edges significantly reduced the energy barrier for N doping, with 12.58 eV lower energy than that in plane of graphite (Fig. 1h and Fig. S3). These results indicated that constructing biochar with micropore-rich and CVs edges was beneficial for improving N doping efficiency and achieving high N coordination number.

In the XRD pattern (Fig. S4) and high-resolution transmission electron microscopy (HRTEM, Fig. 2a) of Fe-N-FPBC, no diffraction peaks and lattice streaks from Fe-containing crystals were observed, and only partial lattice streaks corresponding to the (002) plane of graphitic carbon were found (Fig. S5), indicating the absence of crystalline Fe

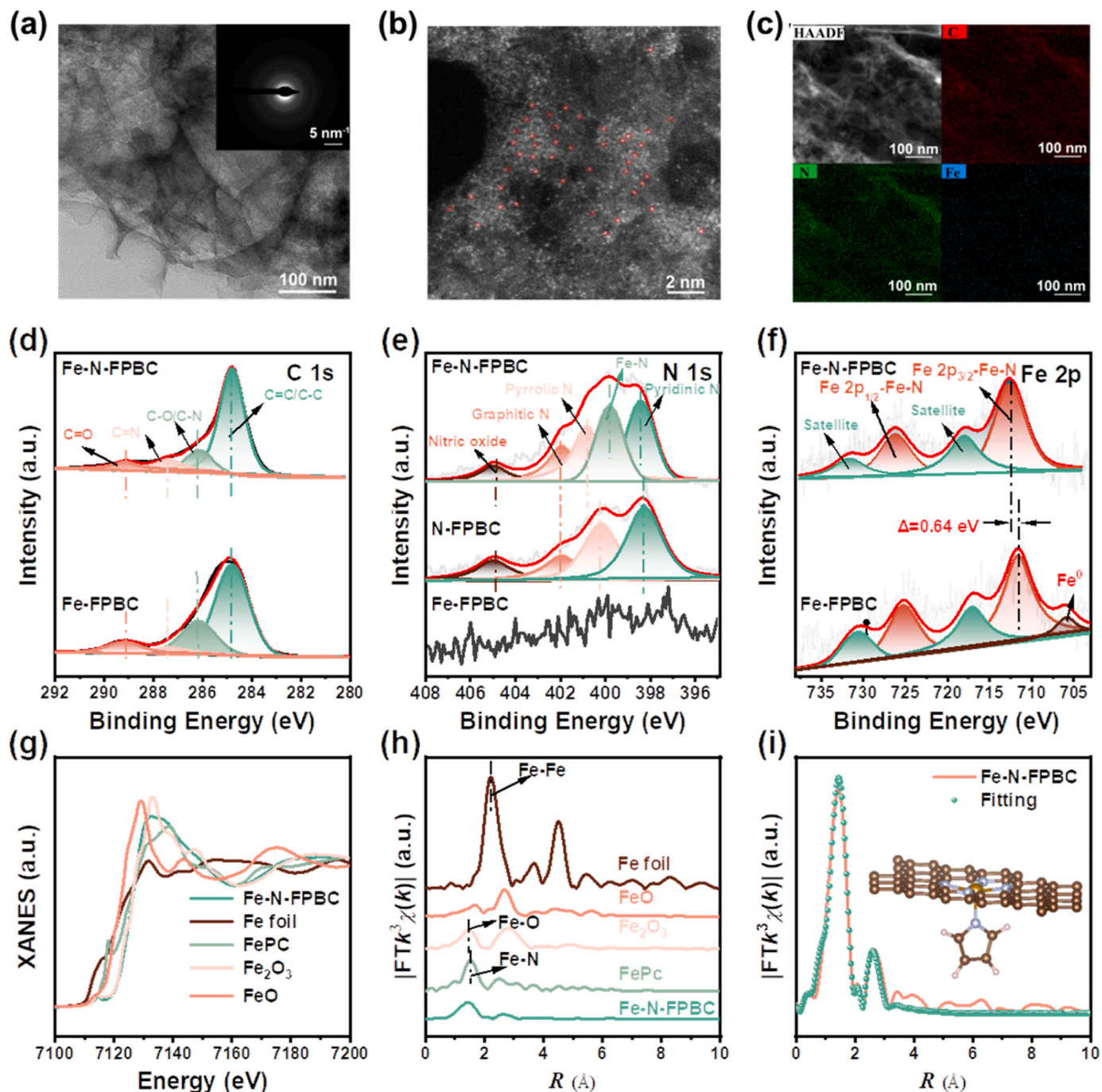


Fig. 2. (a) HRTEM and SAED (Inset) images of Fe-N-FPBC. (b) AC-HAADF-STEM micrograph of Fe-N-FPBC. (c) HAADF-STEM and EDS elemental mapping of Fe-N-FPBC. (d) The C 1s core-level XPS spectra of Fe-FPBC and Fe-N-FPBC. (e) The N 1s core-level XPS spectra of Fe-FPBC, N-FPBC, and Fe-N-FPBC. (f) The Fe 2p core-level XPS spectra of Fe-FPBC and Fe-N-FPBC. (g) Normalized Fe K-edge XANES spectra, (h) Fourier-transformed k^3 -weighted Fe K-edge EXAFS spectra of Fe foil, FePc, Fe_2O_3 , FeO, and Fe-N-FPBC. (i) Fe K-edge EXAFS fitting of Fe-N-FPBC.

species in Fe-N-FPBC. This was further demonstrated by the selected area electron diffraction (SAED, Fig. 2a). In addition, as shown in Fig. 2b, the atomic-level Fe dispersion on Fe-N-FPBC was directly confirmed by the aberration-corrected high-angle annular dark-field scanning transmission electron microscopy (AC-HAADF-STEM). Meanwhile, the EDX element mapping further revealed that Fe and N elements were uniformly distributed on Fe-N-FPBC (Fig. 2c). However, Fe₃O₄ nanoparticles on the surface of Fe-N-PBC and Fe-FPBC could be observed by HRTEM with a lattice spacing of 0.19 nm (Fig. S6), indicating that functional group construction and effective N doping on PBC were essential to prevent the agglomeration of Fe atoms.

The element chemical state of Fe-N-FPBC was analyzed by the X-ray photoelectron spectroscopy (XPS). The wide-scan XPS spectrum (Fig. S7) indicated the presence of C, N, O, and Fe elements in Fe-N-FPBC. In the C 1s core-level XPS spectrum (Fig. 2d), the signal of Fe-N-FPBC could be convoluted into four peaks, where the increased proportion of C=N compared to that of Fe-FPBC (9.15% vs 5.35%) indicated successful N doping into the carbon layer. As shown in Fig. 2e, the

N 1s core-level XPS spectrum of N-FPBC was convoluted to four peaks assigned to pyridine N, pyrrole N, graphite N, and oxide N, among which pyridine N accounted for the highest proportion (41.16%) (Table S5) [26–28]. Meanwhile, the Fe-N peak appeared in the N 1s spectrum of Fe-N-FPBC (Fig. 2e), indicating the coordination of pyridine N with Fe [29,30]. In the Fe 2p XPS spectrum (Fig. 2f), the Fe-N peaks of Fe-N-FPBC shifted to a higher binding energy by 0.64 eV compared with that of Fe-FPBC, indicating the increased Fe valence. This could be due to the coordination of the Fe atom with more N atoms in Fe-N-FPBC, resulting in a decrease in the local electron density of Fe [31]. Moreover, the appearance of an Fe⁰ peak in Fe-FPBC was attributed to the lack of coordination anchoring of N atoms, which resulted in the migration and agglomeration of Fe atoms at high temperatures, ultimately forming low-valence Fe nanoparticles. This interpretation was consistent with the HRTEM results (Fig. S6).

To investigate the Fe coordination environment in Fe-N-FPBC, X-ray absorption fine structure (XAFS) spectroscopy was employed. The X-ray absorption near-edge structure (XANES) spectrum (Fig. 2g) showed that

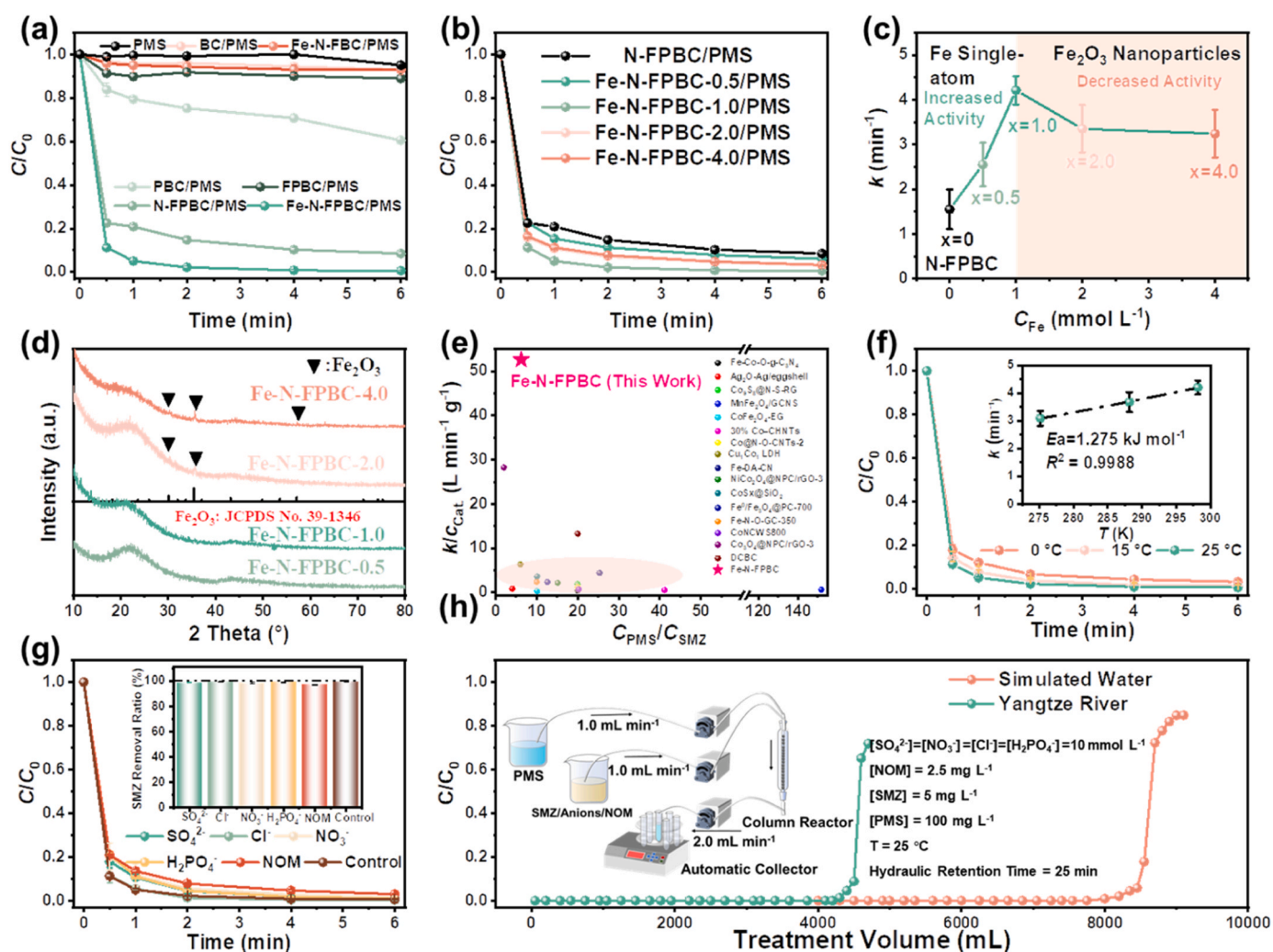


Fig. 3. (a) Degradation kinetic curves of SMZ by PMS alone and BC, Fe-N-FBC, PBC, FPBC, N-FPBC, and Fe-N-FPBC via PMS activation. (b) Degradation kinetic curves of SMZ by Fe-N-FPBC-*x* (*x* = 0–4.0) via PMS activation. (c) The effect of C_{Fe} on k values in Fe-N-FPBC-*x* (*x* = 0–4.0). (d) XRD patterns of Fe-N-FPBC-*x* (*x* = 0–4.0). (e) Catalytic efficiency comparison between Fe-N-FPBC and the previously reported catalysts in the degradation efficiency of SMZ via PMS activation. (f) Degradation kinetic curves of SMZ by Fe-N-FPBC activated PMS at different temperatures (Inset: fitting results of k value and reaction temperature (T) through Arrhenius equation). (g) The effects of anions and NOM on the degradation kinetics curves and removal ratio (Inset: of SMZ by Fe-N-FPBC). (h) Schematic diagram of catalytic column reactor (Inset: employing Fe-N-FPBC loaded on absorbent cotton for SMZ degradation in the simulated (Reaction conditions were listed inside) and real wastewater treatment. Reaction conditions for (a, b, c, d, e, f, and g): [Catalyst] = 80 mg L⁻¹, [PMS] = 0.495 mmol L⁻¹ (75 mg L⁻¹), [SMZ] = 78.967 μmol L⁻¹ (20 mg L⁻¹), pH₀ = 5.2, T_0 = 25 °C (if need). For (f): T_0 = 0, 15 and 25 °C. For (g): [SO₄²⁻] = [Cl⁻] = [NO₃⁻] = [H₂PO₄⁻] = 100 mmol·L⁻¹, [NOM] = 5 mg L⁻¹, T_0 = 25 °C.

the Fe rising edge of Fe-N-FPBC was close to that of Fe_2O_3 , indicating that the Fe oxidation state was about +3. The Fe K-edge Fourier transform (FT) extended X-ray absorption fine structure (EXAFS) spectrum (Fig. 2h) showed a strong peak associated with the Fe-N first coordination shell at 1.47 Å. What's more, only one intensity maximum at 5.2 Å assigned to Fe-N bond was observed from the wavelet transform (WT) contour plot (Fig. S8), indicating that Fe atom was dispersed on Fe-N-FPBC in the form of Fe-N coordination [32]. Furthermore, the quantitative Fe coordination structure was studied by EXAFS fitting (Fig. 3i). Specifically, the average N coordination number of Fe was 5.1 ± 0.3 , and the corresponding average Fe-N bond length was 1.94 ± 0.01 Å (Table S6), inferring that one Fe atom was coordinated with five N atoms to form the FeN_5 coordination structure.

3.2. Catalytic performance and low-temperature resistance

SMZ was used as a model pollutant to evaluate the catalytic performance of Fe-N-FPBC (Fig. 3a). The degradation efficiency of SMZ by PMS alone was only 4.96% within 6 min, indicating that the oxidation capacity of PMS was weak. Both BC and Fe-N-FBC prepared without constructing porous structure degraded less than 10% of SMZ by activated PMS within 6 min. In contrast, PBC, N-FPBC and Fe-N-FPBC with constructing pores increased the degradation efficiency of SMZ to 39.49%, 91.44% and 100%, respectively. Moreover, the adsorption capacities of Fe-N-FBC and Fe-N-FPBC for SMZ within 30 min were 9.35 mg g^{-1} and 220.38 mg g^{-1} , respectively (Fig. S9). These results indicated that the construction of a porous-rich structure was beneficial for improving the mass transfer efficiency among PMS-catalyst-SMZ and increasing the adsorption capacity of SMZ, thus accelerating the catalysis. More importantly, as shown in Fig. S10, Fe-N-FPBC exhibited higher catalytic activity compared to Fe-N-PBC and Fe-FPBC with first-order kinetic constants (k) of 4.21, 1.87, and 1.60 min^{-1} , respectively. This result indicated that the cascade process of constructing functional groups and N-doping was essential to improve the catalytic activity. In addition, the efficiency of Fe-N-FPBC activated O_2 and direct degradation of SMZ without PMS were only 6.98% and 6.71%, respectively (Fig. S11). Therefore, Fe-N-FPBC could hardly activate O_2 and directly degrade SMZ and the degradation of SMZ primarily originated from the activation of PMS.

The effect of Fe amount in Fe-N-FPBC- x ($x = 0\text{--}4.0$) on the SMZ degradation kinetics was investigated (Fig. 3b). As shown in Fig. 3c, the relationship between Fe^{3+} adsorption solution concentration (C_{Fe}) and k values exhibited a volcano distribution. Specifically, as C_{Fe} increased from 0 to 1.0 mmol L^{-1} , k increased from 1.55 to a maximum of 4.21 min^{-1} due to the increased Fe sites, but decreased to 3.24 min^{-1} instead when C_{Fe} further increased to 4.0 mmol L^{-1} . Notably, when $C_{\text{Fe}} \geq 2 \text{ mmol L}^{-1}$, the materials showed XRD diffraction peaks of Fe nanoparticle (Fig. 3d), suggesting the higher catalytic activity of single-atom Fe over Fe nanoparticle [32]. Similarly, the relationship between the pyrolysis temperature and k values also showed a volcano distribution (Fig. S12a-b). The maximum k value of 4.21 min^{-1} was obtained when the temperature was 800°C , but k was decreased to 3.22 min^{-1} with further increase in temperature due to the formation of Fe nanoparticle confirmed by XRD (Fig. S13) [33]. Moreover, as shown in Fig. 3e and Table S7, the k value normalized to the catalyst dosage reached $52.63 \text{ L min}^{-1} \text{ g}^{-1}$, which was 1.86–145.37 times the reported values under comparable reaction conditions.

In many regions, the water temperature approached 0°C during winter. The ability of a catalyst to function efficiently at low temperatures determined whether external heating or an increase in reagent dosage was necessary to maintain catalytic efficiency [34]. Therefore, the catalytic efficiency of Fe-N-FPBC at low temperatures was evaluated. To evaluate the low-temperature resistance of the catalyst, the reaction temperature (T) was reduced from 25 to 0°C . As shown in Fig. 3f, the SMZ removal rate of Fe-N-FPBC did not decrease significantly. Notably, the catalyst-dose-normalized k still reached $38.75 \text{ L min}^{-1} \text{ g}^{-1}$ at 0°C ,

which far outperformed the values reported for most catalysts at 25 and 30°C (Table S7). In addition, the apparent activation energy (E_a , kJ mol^{-1}) of SMZ degradation was calculated according to the Arrhenius equation:

$$k = Ae^{-\frac{E_a}{RT}} \quad (1)$$

Where A and R were the frequency factor (min^{-1}) and molar gas constant ($8.314 \text{ J mol}^{-1} \text{ K}^{-1}$), respectively. The E_a value of Fe-N-FPBC was only $1.275 \text{ kJ mol}^{-1}$, much lower than the E_a values of $18.4\text{--}59.0 \text{ kJ mol}^{-1}$ for previously reported catalysts (Table S7). Because the E_a values of surface-reaction-controlled reaction and diffusion-controlled reaction were $> 25 \text{ kJ mol}^{-1}$ and $10\text{--}13 \text{ kJ mol}^{-1}$, respectively [34–36], the ultralow E_a of Fe-N-FPBC indicated that the surface reaction on the FeN_5 sites and mass transfer proceeded very quickly.

3.3. Anti-interference ability and reusability

As shown in Fig. 3g, although the high concentration of anions (NO_3^- , Cl^- , H_2PO_4^- , and SO_4^{2-}) and NOM slowed down the degradation rate, they did not significantly reduce the degradation efficiency of SMZ within 6 min, indicating that the contribution of free radicals to SMZ degradation was not significant [37]. In addition, according to our previous work, a catalytic column reactor was constructed by dispersing Fe-N-FPBC onto a cotton column for dynamic SMZ removal from simulated and real waters (Fig. 3h, inset) [34]. The PMS solution and SMZ were pumped simultaneously into the column reactor for continuous treatment. Surprisingly, the cumulative water treated by the catalytic column reactor for simulated and real wastewater was 7.75 L and 4.2 L, respectively. The amount of pollutants that could be treated by a unit mass of catalyst was up to $1.91 \text{ mmol}_{\text{SMZ}} \text{ g}_{\text{cat}}^{-1}$ and $1.04 \text{ mmol}_{\text{SMZ}} \text{ g}_{\text{cat}}^{-1}$ for simulated and real wastewater, respectively. Meanwhile, the discharged SO_4^{2-} was only about 126.31 mg L^{-1} , lower than the national sulfate emission standard (250 mg L^{-1}) [38].

The effect of reaction parameters on the degradation of SMZ by Fe-N-FPBC was further investigated (Table S8 and Fig. S14a-c). The removal efficiency of SMZ increased with the increase in the amount of PMS and Fe-N-FPBC. In the pH range of $3.0\text{--}10.0$, the degradation efficiency of Fe-N-FPBC for SMZ gradually decreased with increasing pH (Fig. S15a), and the adsorption capacity for SMZ also decreased (Fig. S15b). This could be attributed to the low point of zero charge value ($\text{pH}_{\text{PZC}} = 2.58$ eV) of Fe-N-FPBC (Fig. S16), which increased the electrostatic repulsion between the catalyst surface and PMS or SMZ as the solution pH increased [17]. Additionally, Fe-N-FPBC was effective in the rapid degradation of various pollutants, like phenol, bisphenol A (BPA), methyl orange (MO), and ofloxacin (OFL) (Fig. S17). The total organic carbon (TOC, Fig. S18) analysis showed that the mineralization rate of SMZ in the Fe-N-FPBC/PMS system was 58.27% within 10 min. In addition, the properties of the Fe-N-FPBC before and after the reaction were evaluated in Fig. S19. Meanwhile, the catalytic activity of the used Fe-N-FPBC sample was restored by simple thermal regeneration (Fig. S20), and the degradation efficiency of SMZ was still over 98% after four cycles (Fig. S21), with almost no Fe leakage (Fig. S22). Moreover, the Fe-N-FPBC/PMS system demonstrated highly efficient sterilization performance, achieving 100% elimination of 1×10^5 CFU of *E. coli* within 5 min (Text. S4 and Fig. S23).

3.4. Degradation pathway and toxicity evaluation

Analyzing the toxicity of intermediates was crucial for evaluating the effectiveness of Fenton-like oxidative degradation. In the Fe-N-FPBC/PMS system, the liquid chromatography-mass spectrometry (LC-MS) analysis (Table S9) was used to detect the degradation intermediates of SMZ, and the degradation pathways were deduced in Fig. 4a. Meanwhile, developmental toxicity and bioaccumulation factors, two key

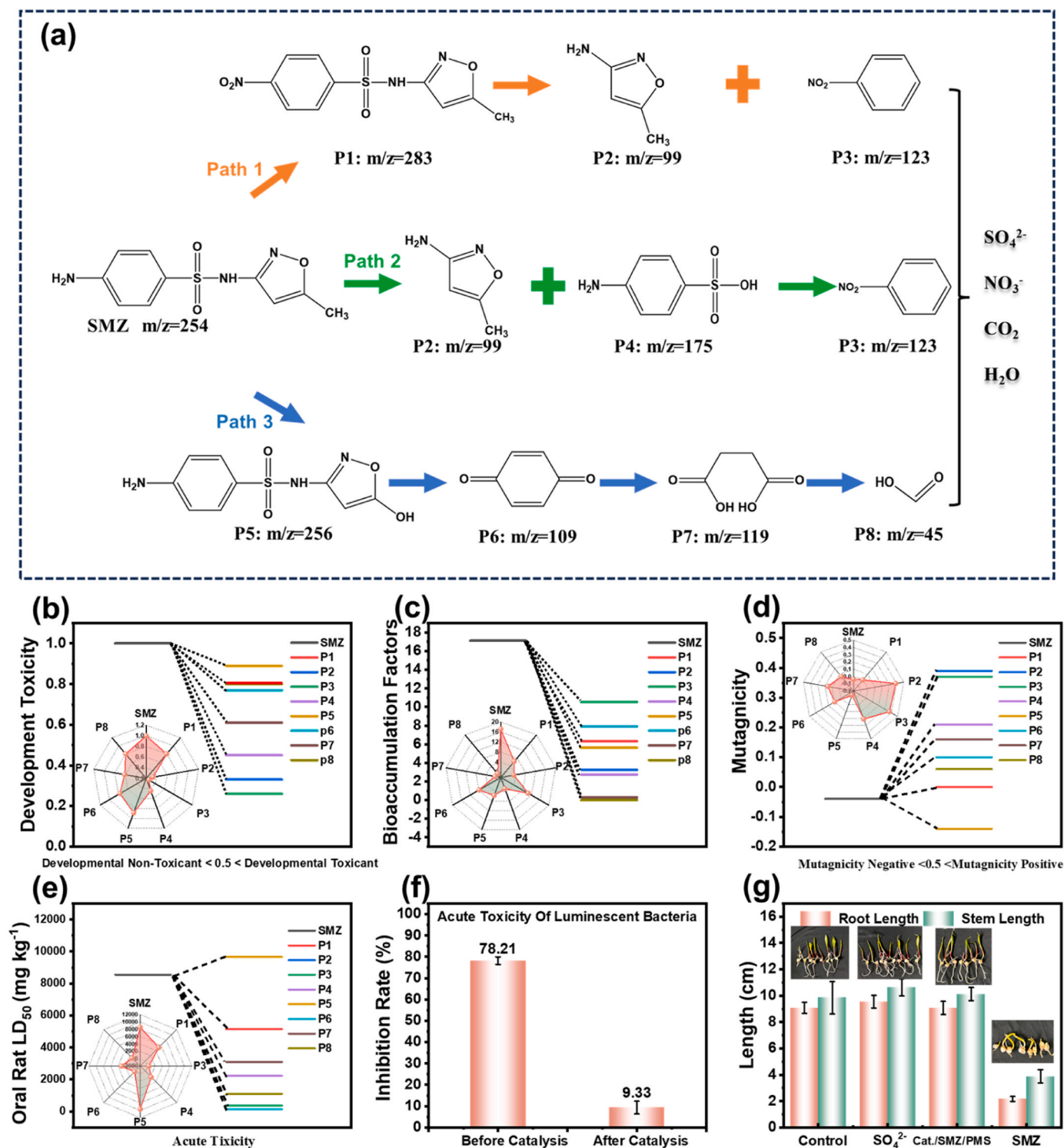


Fig. 4. (a) Possible degradation pathway of SMZ by Fe-N-FPBC via PMS activation. (b) The development toxicity, (c) bioaccumulation factors, (d) mutagenicity, and (e) acute toxicity of oral rat LD₅₀ results of SMZ and intermediates by the T.E.S.T software. (f) Luminescent bacteria acute toxicity of SMZ and its degradation intermediates before and after catalytic reaction. (g) Average root length and stem length of maize seedlings cultivated by ultrapure water, SO_4^{2-} solutions, SMZ solutions before and after catalysis. Reaction conditions for (a and d): [Catalyst] = 80 mg L⁻¹, [PMS] = 0.495 mmol L⁻¹ (75 mg L⁻¹), [SMZ] = 78.967 μ mol L⁻¹ (20 mg L⁻¹), pH₀ = 5.2, T₀ = 25 °C.

toxicity indicators, were predicted using the Toxicity Estimation Software Tool (T.E.S.T.) [39]. As shown in Fig. 4b-c, the developmental toxicity and the bioaccumulation factors of all intermediates were significantly lower than that of SMZ, indicating that the biological toxicity of intermediates was reduced. Furthermore, all intermediates except P5 showed increased mutagenicity (Fig. 4d), but all values less

than 0.5 exhibiting negative mutagenicity. For the acute toxicity of oral LD₅₀ in rats, all intermediates from SMZ displayed the lower values than SMZ (8549.94 mg kg⁻¹) except P5 (Fig. 4e). This indicated an increase in the acute toxicity of the intermediates for rats. In addition, in order to further study the evolution of acute toxicity of SMZ to microorganisms, untreated and treated SMZ solutions were used as nutrient solution to

culture luminescent bacteria (Fig. 4f) [40]. It was obvious that the inhibition rate of SMZ solution for luminescent bacteria was 78.21% before treatment, but only 9.33% after treatment. The results indicated that the acute toxicity of SMZ degradation intermediates to luminescent bacteria was reduced. Additionally, to directly demonstrate the toxicity reduction of intermediates, corn seeds cultivation toxicity experiments were conducted and the dynamic process of corn seed germination and seedling growth was also recorded. The experimental results showed that the SMZ storage solution severely inhibited seed development compared to the control, with root length and stem length of seedlings being only 2.18 cm and 3.88 cm after 8 days, respectively. However, the SMZ reaction solution-cultured corn seeds barely inhibited seed development (Fig. S24 and Fig. 4d), with seedlings root length and stem length of 9.08 cm and 9.85 cm, respectively. Overall, the catalysis of the Fe-N-FPBC/PMS system could not only effectively remove SMZ, but also weaken the effluent toxicity.

3.5. Determination of catalytic path

Quenching tests were performed to determine the dominant reactive oxygen species (ROSs) responsible for the degradation of the SMZ in the Fe-N-FPBC/PMS system. The ethanol could simultaneously quench $\bullet\text{OH}$ and $\text{SO}_4^{\bullet-}$ with high activity ($k(\text{SO}_4^{\bullet-}, \text{EtOH}) = 1.6\text{--}1.77 \times 10^7 \text{ M}^{-1} \text{ s}^{-1}$ and $k(\bullet\text{OH}, \text{EtOH}) = 1.2\text{--}2.8 \times 10^9 \text{ M}^{-1} \text{ s}^{-1}$), while tert-butanol (TBA) without $\alpha\text{-H}$ was only highly reactive towards $\bullet\text{OH}$ ($k(\bullet\text{OH}, \text{TBA}) = 3.8\text{--}7.6 \times 10^8 \text{ M}^{-1} \text{ s}^{-1}$) [41,42]. As shown in Fig. 5a, the addition of EtOH and TBA had a negligible effect on the removal of SMZ, which ruled out the involvement of $\bullet\text{OH}$ and $\text{SO}_4^{\bullet-}$ in the degradation of SMZ. L-histidine (LH) and p-benzoquinone (PBQ) have good reactivity with $^1\text{O}_2$ and $\text{O}_2^{\bullet-}$, respectively [43]. The addition of LH significantly reduced the activity of the catalyst, indicating that $^1\text{O}_2$ might exist. Additionally, the lifetime of $^1\text{O}_2$ in heavy water (D_2O , $t_{\text{D}_2\text{O}} = 20 \text{ }\mu\text{s}$) and TBA ($t_{\text{TBA}} = 34 \text{ }\mu\text{s}$) were longer than that in H_2O ($t_{\text{H}_2\text{O}} = 2 \text{ }\mu\text{s}$), so for the degradation reaction dominated by $^1\text{O}_2$, the contaminant degradation could be accelerated by replacing H_2O with D_2O or TBA solution [34,44]. On the

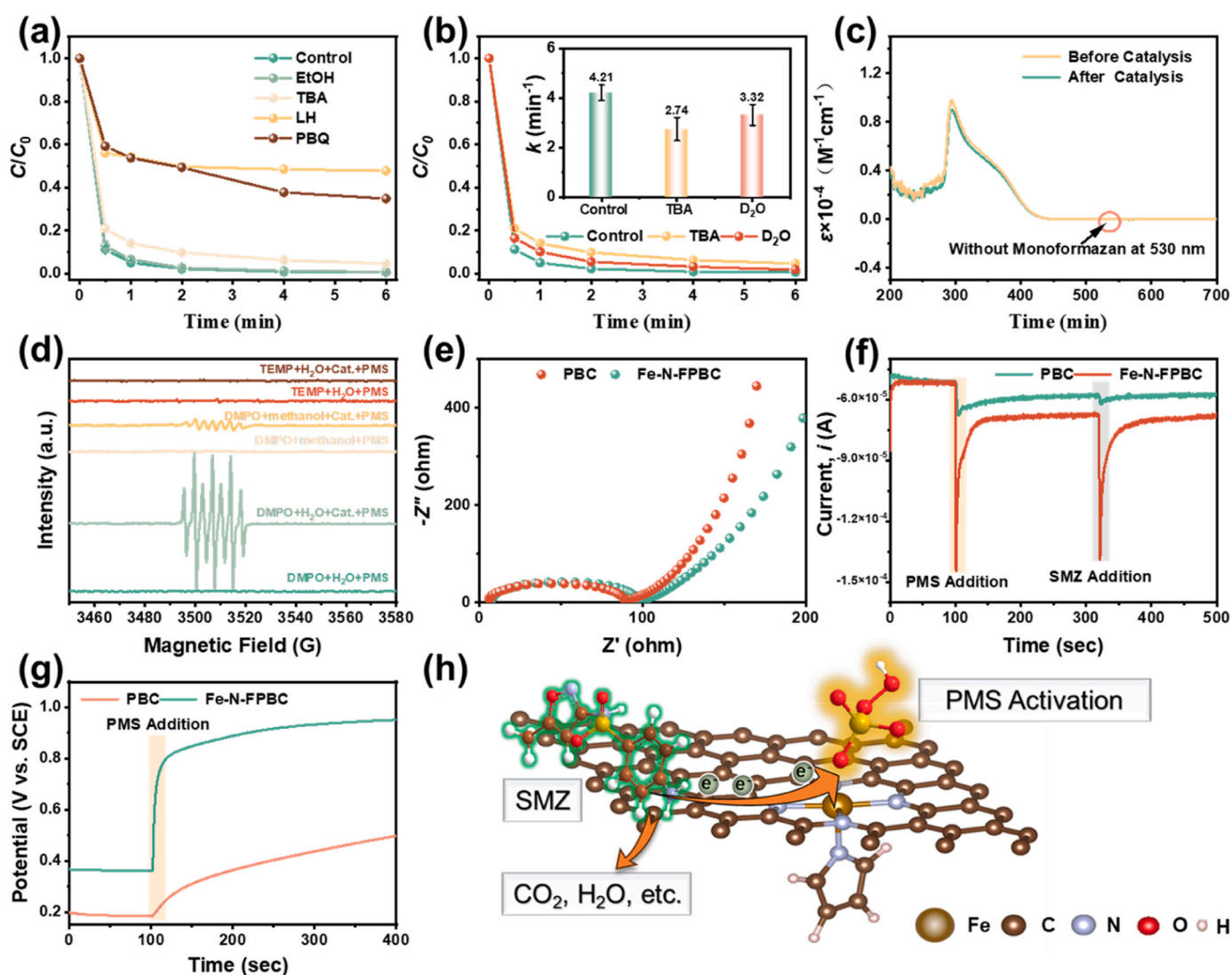


Fig. 5. (a) Effects of ROSs quenchers on SMZ degradation in Fe-N-FPBC/PMS system. (b) Effects of D_2O and TBA solution (0.2 mol L^{-1}) on the degradation kinetics and k value (Inset) of SMZ in Fe-N-FPBC/PMS system. (c) UV-Vis spectra of NBT solutions before and after catalysis in Fe-N-FPBC/PMS system. (d) The EPR spectra of PMS activation by Fe-N-FPBC under different conditions with DMPO or TEMP as the trapping agents. (e) Nyquist plots of PBC and Fe-N-FPBC coated working electrodes. Inset: equivalent fitting circuit. (f) Chronoamperometry and (g) Chronopotentiometry curves with adding PMS and SMZ solutions in PBC and Fe-N-FPBC coated working electrodes. (h) Schematic illustration of the catalyst-mediated electron-transfer path. Reaction conditions for (a, b, c, d): [Catalyst] = 80 mg L^{-1} (if needed), [PMS] = $0.495 \text{ mmol L}^{-1}$ (75 mg L^{-1}), [SMZ] = $78.967 \text{ }\mu\text{mol L}^{-1}$ (20 mg L^{-1}) (if needed), $\text{pH}_0 = 5.2$, $T_0 = 25 \text{ }^\circ\text{C}$. [EtOH] = [TBA] = 0.2 mol L^{-1} , [PBQ] = [LH] = 0.02 mol L^{-1} . [DMPO] = 0.1 mol L^{-1} , [TEMP] = 0.02 mol L^{-1} . For (f, g), added PMS: 0.375 mL , 20 g L^{-1} , added SMZ: 0.5 mL , 100 mg L^{-1} .

contrary, when D₂O and TBA solution were used as the reaction media, the removal rates of SMZ were lower than that in H₂O, and the *k* values decreased by 34.91% and 21.14% (Fig. 5b), respectively, so ¹O₂ could be excluded. Additionally, the addition of PBQ reduced the catalytic activity of the reaction, indicating the possible presence of O₂^{•−}. NBT can react with O₂^{•−} to generate monoformazan, which possessed the absorption maximum at 530 nm in the UV-Vis spectrum [34]. However, no monoformazan peak appeared after catalysis (Fig. 5c), so the existence of O₂^{•−} in the reaction process was excluded. It was found that the addition of PBQ and LH significantly reduced the adsorption amount of SMZ onto Fe-N-FPBC (Fig. S25), which was attributed to the competition between PBQ/LH and SMZ for adsorption sites on the catalyst surface. In addition, according to previous reports, PBQ and LH can react directly with PMS [45]. Therefore, it was reasonable to speculate that the reduced catalytic efficiency might be attributed to the occupation of SMZ adsorption sites on Fe-N-FPBC and partial consumption of PMS by PBQ and LH. As shown in Fig. 5d, the ROSSs was further revealed by electron paramagnetic resonance (EPR). When DMPO was used as the ROSSs trapping reagent, PMS alone did not release any signal, but after adding Fe-N-FPBC, typical seven peaks of 5,5-dimethyl-2-pyrrolidone-N-oxyl (DMPOX) appeared with peaks intensity of 1:2:1:2:1:2:1, indicating SMZ removal in the Fe-N-FPBC/PMS system likely followed a non-radical pathway [43,46]. When the reaction medium was changed from water to methanol, the typical peak of O₂^{•−} was not captured, but the peak of DMPOX with weakened intensity appeared, which was attributed to the inhibition of the adsorption of DMPO on the catalyst by methanol [47]. TEMP is usually used to capture ¹O₂ because TEMP can react with ¹O₂ to form TEMPN (2,2,6,6-tetramethylpiperidine-N-oxyl) [48]. With the addition of PMS only, a faint characteristic triplet peak of TEMPN was captured due to the slow self-decomposition of PMS to generate ¹O₂ [49]. However, after adding Fe-N-FPBC, the signal of ¹O₂ disappeared, which proved that the generation route of ¹O₂ was hindered and replaced by another route (Fig. 5b). What's more, high-valent iron species (e.g. Fe^{IV}=O) were also considered as the possible ROSSs to degrade organic pollutants using a Fe-based catalyst [50,51]. Phenyl-methyl sulfoxide (PMSO) can be oxidized by Fe^{IV}=O to form phenyl-methyl sulfoxide (PMSO₂) by oxygen transfer reaction [44,52]. In the high-performance liquid chromatography (HPLC) spectra, the peaks of PMSO and PMSO₂ standard samples could be observed at 6.67 and 12.07 min, respectively (Fig. S26). However, PMSO₂ was not detected in Fe-N-FPBC/PMS/PMSO system, indicating that there was no Fe^{IV}=O in this process.

The catalyst-mediated electron transfer process might be another effective mechanism to eliminate pollutants, and the mechanism occurred preferentially when the catalyst had high electrical conductivity and high adsorption capacity for pollutants [43,53]. To investigate this mechanism, the electrochemical impedance spectroscopy (EIS) of PBC and Fe-N-FPBC were measured to evaluate the conductivity (Fig. 5e). The semicircle diameter and linear part slope of Nyquist plots represented the charge-transfer resistance (*R*_{ct}) and mass transfer resistance, respectively [54]. Fe-N-FPBC and PBC had a similar semicircular diameters and *R*_{ct} of approximately 91.0 Ω, which was lower than that of comparable reported carbon composites (Table S10), indicating the good electrical conductivity of Fe-N-FPBC. Meanwhile, the adsorption efficiency of Fe-N-FPBC for SMZ within 30 min was as high as 88.15%, and the maximum adsorption capacity was 220.38 mg g^{−1}, which laid a good foundation for the catalyst-mediated electron transfer process to eliminate pollutants. As shown in Fig. 5f, the chronoamperometry curve recorded the current change in the catalytic reaction process. When PMS was added, the output current increased instantaneously, indicating that PMS and Fe-N-FPBC rapidly formed bond and exchanged electrons [55]. A similar current change occurred after the addition of SMZ, indicating that the catalyst could rapidly extract electrons from SMZ. However, the intensity of current change in PBC was relatively lower than Fe-N-FPBC, which might be attributed to the fact that Fe-N-FPBC had more active Fe single-atom sites. According

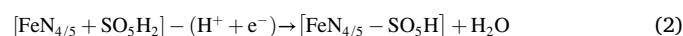
to the chronopotentiometry analysis in Fig. 5g, the potential of the Fe-N-FPBC electrode rapidly increased to approximately 1.0 V following the addition of PMS. This result suggested that the Fe-N-FPBC and PMS quickly combined to form a complex, leading to an increase in the redox potential and facilitating the acceptance of additional electrons [53]. In the Fe-N-FPBC/PMS/SMZ system, the addition of SMZ could accelerate PMS consumption (Fig. S27). In addition, in-situ Raman spectroscopy was used to reveal the surface chemical evolution of Fe-N-FPBC after the addition of PMS and SMZ (Fig. S28). After adding Fe-N-FPBC to the PMS solution, the formation of activated PMS* on the surface of Fe-N-FPBC could be observed at ~832 cm^{−1} [53]. However, after adding SMZ to the mixed phase of PMS and Fe-N-FPBC, the PMS* signal disappeared, demonstrating that the complex PMS* formed by PMS and Fe-N-FPBC was an active species for SMZ degradation [53]. Furthermore, salt bridge experiments have demonstrated that the catalyst mediated the flow of current from SMZ to PMS, achieving the degradation of SMZ (Fig. S29). Thus, the efficient electron transfer channel was constructed as SMZ (electron donor)-Fe-N-FPBC (conducting medium)-PMS (electron acceptor) (Fig. 5h), allowing the electrons in the adsorbed SMZ to be extracted and flow to the region with high redox potential for efficient degradation of SMZ.

3.6. Catalytic active center recognition

Identifying the active centers was crucial for understanding the above-mentioned electron transfer process. To explore the contribution of Fe single-atom sites in activating PMS, the poisoning experiment using SCN[−] was performed, as SCN[−] could strongly bind with Fe atom to inhibit the binding of PMS [45]. SCN[−] significantly inhibited the catalytic efficiency of Fe-N-FPBC, and the degradation efficiency was only 19.69% within 6 min, confirming that the Fe single-atom site was the active center for activating PMS (Fig. S30). On the contrary, the homogeneous Fe³⁺/PMS system with the Fe content equal to that of Fe-N-FPBC hardly degraded SMZ (Fig. S31), indicating that the coordination environment of the biochar support enabled Fe atoms to effectively activate PMS.

DFT calculations were used to further explain the mechanism of the catalytic degradation process. Based on the above results, structural models of PMS adsorption on graphene with FeN₄ site and FeN₅ site (Fe-N-FPBC) were constructed (Fig. 6a), respectively. The FeN₅ site was represented as the FeN₄ site with an axial pyrrole ligand [34]. Difference charge density analysis demonstrated that the -SO₃H group could accumulate a large number of electrons from the FeN₄ and FeN₅ sites (Fig. 6a), facilitating the activation of PMS. It was worth noting that in comparison to the FeN₄ site, the FeN₅ site demonstrated a relatively moderate adsorption energy (*E*_{ads}) for PMS (−2.65 eV vs −2.92 eV). Moreover, the density of states (DOS) of the Fe center and O atom before and after the adsorption of PMS on the Fe sites were also calculated in the Fig. 6b-c. The d-band centre of Fe on the FeN₅ site was further away from the Fermi energy level than that of FeN₄ site (−3.90 eV vs −3.31 eV), favouring the desorption of PMS product molecules [12]. Additionally, the projected density of states (PDOS) between Fe 3d and O 2p orbitals showed more overlap compared to FeN₄ site, implying that FeN₅ site could activate the PMS better [12].

The possible steps of PMS activation were investigated on FeN₄ and FeN₅ models. Based on our previous work, it was considered that the PMS molecule initially bonded with the metal center to form a suspended -SO₃H group as the active oxidant [34]. Inspired by the established computational hydrogen electrode (CHE) model, we proposed four reactions to evaluate the energy change (Eqs. 2–5), where the energy of the proton-electron pair could be estimated as one-half of the energy of H₂, and the energy change of the species during the reaction was calculated by DFT (Fig. 5e).



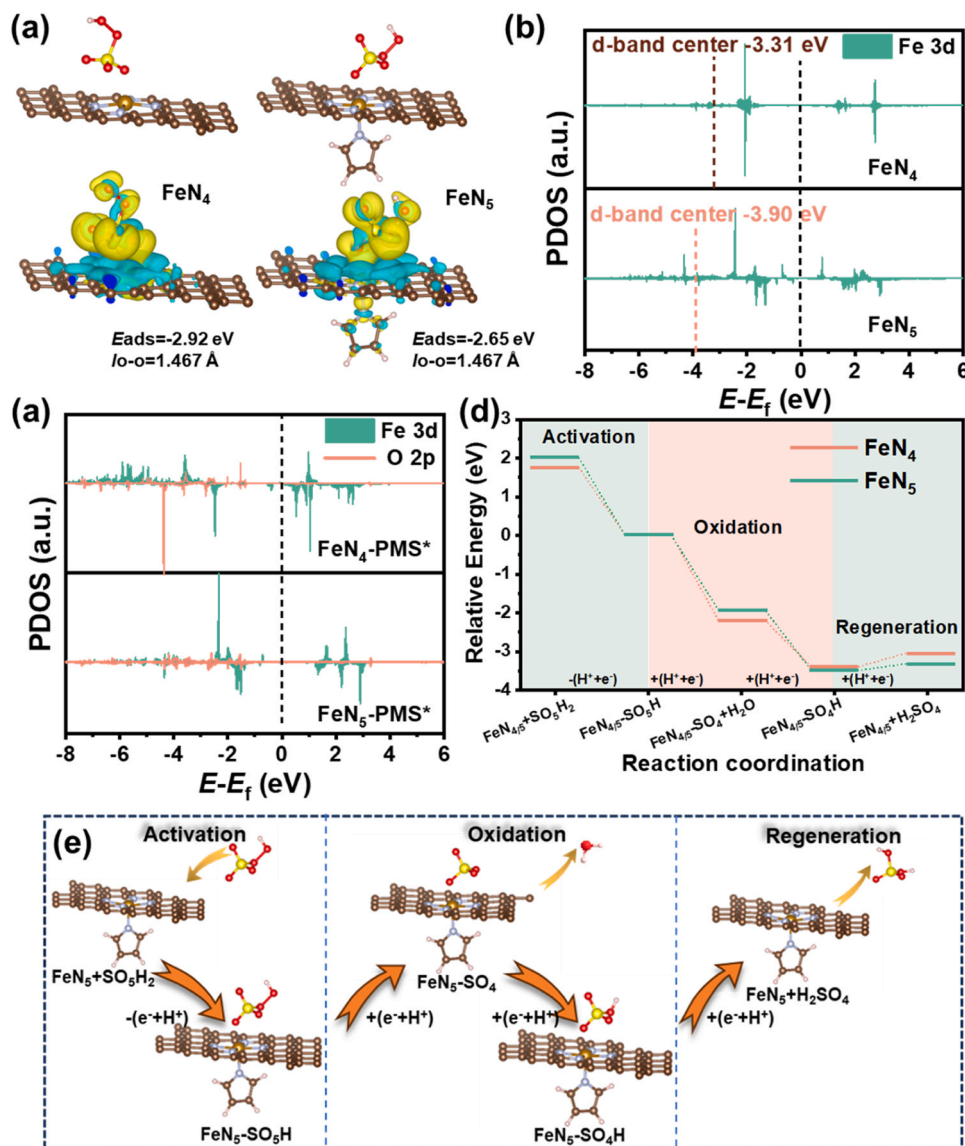
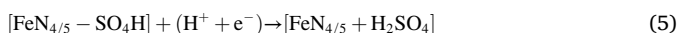
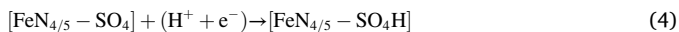
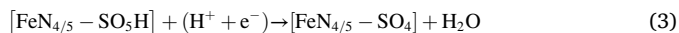


Fig. 6. Theoretical investigation of PMS-activated Fe-N-FPBC with FeN₅ sites. (a) Structural models of PMS adsorption FeN₄ and FeN₅ sites and corresponding difference charge density (DCD) results. Blue and yellow represented charge depletion and accumulation, respectively. The isosurface value was 0.001 e Å⁻³. (b-c) Density of states (DOS) of Fe centers and O atoms before and after adsorption of PMS by FeN₄ and FeN₅ sites. (d) Gibbs free energy diagrams of the catalytic oxidation processes on FeN₄ and FeN₅ sites. (e) Species evolution of PMS on FeN₅ site.



In the activation, PMS bound the single-atom Fe center to form the active species. As shown in Fig. 6 d, the FeN_{4/5}-SO₅H group achieved pollutant degradation through a two-electron transfer process. In the oxidation step, the O-O bond of FeN_{4/5}-SO₅H was cleaved to form the [FeN_{4/5}-SO₄] intermediates, and both states were observed to have highly negative relative energies. Subsequently, the [FeN_{4/5}-SO₄] states further captured electrons to form [FeN_{4/5}-SO₄H] state, resulting in a greater relative energy decrease in the structures. It was shown that the [FeN_{4/5}-SO₄] transition states was crucial in the oxidation process. Moreover, the [FeN₅-SO₄H] state exhibited a larger relative energy change compared to the [FeN₄-SO₄H] states (-1.57 eV vs -1.20 eV), suggesting that FeN₅ combined with -SO₅H still retained a strong oxidation capacity. The highly coordination-unsaturated FeN₄ site

required 0.17 eV more energy to desorb -SO₄H than the FeN₅ site, indicating that the regeneration of the FeN₅ site was thermodynamically more favourable. In other words, the FeN₅ sites only needed to overcome the lower-energy-barrier than FeN₄ to achieve single-atom sites regeneration. This could be the reason for the efficient activation of PMS by Fe-N-FPBC (FeN₅) at room and low temperatures and its ultra-fast kinetic properties.

As previously mentioned, [FeN_{4/5}-SO₄] species played a crucial role in the overall process, and active [FeN_{4/5}-SO₄] states were likely to contribute to the oxidation performance. Based on bader charge analysis, the charges of Fe center were +1.054 |e| and +1.224 |e| in FeN₄ and FeN₅, respectively. In the [FeN_{4/5}-SO₄] states, the Fe charges of FeN₄ and FeN₅ were +1.321 |e| and +1.306 |e|, respectively. Meanwhile, the charges of -SO₄ were -1.306 |e| and -1.249 |e|, respectively. The charge difference between Fe and -SO₄ (ΔQFe-SO₄) can serve as a metric to assess the extent of charge transfer [34]. Notably, FeN₅ transferred less charges to -SO₄ than FeN₄, ΔQFe-SO₄ were 2.555 |e| and 2.627 |e|, respectively, suggesting that the axially coordinated pyrrole-N ligand of FeN₅ could act as an electron store, buffering electronic

changes in the Fe center to stabilize the active intermediate state. Therefore, the less charge feedback from Fe to $-\text{SO}_4$ at the critical $[\text{FeN}_5\text{-SO}_4]$ transition state was thermodynamically favorable for the trapping of electrons from pollutants.

4. Conclusion

In this paper, a cascade regulation strategy was proposed for the preparation of highly efficient single-atom Fe-based catalysts (Fe-N-FPBC) by anchoring atomically dispersed Fe-N₅ sites on microporous and defect-rich biochar support. Fe-N-FPBC mediated the electron transfer between PMS and SMZ, achieving ultra-fast kinetic performance for SMZ degradation. The catalyst-dosage-normalized kinetic constant was up to $52.63 \text{ L min}^{-1} \text{ g}^{-1}$, which was 1.86–145.37 times the reported values. Meanwhile, Fe-N-FPBC showed high resistance to the interference of anions, low temperature (0 °C), and natural organic matter. The tower reactor loaded with Fe-N-FPBC achieved zero SMZ discharge for 4.2 L in real wastewater treatment, and the amount of pollutants that could be treated by a unit mass of catalyst was up to $1.04 \text{ mmol}_{\text{SMZ}} \text{ g}_{\text{cat}}^{-1}$. The Fe-N-FPBC/PMS system demonstrated highly efficient sterilization performance. Moreover, the weakened toxicity of SMZ degradation intermediates of the Fe-N-FPBC/PMS system was verified using the T.E.S.T software predictions, acute toxicity test of luminescent bacteria, and corn seeds cultivation toxicity experiments. DFT calculations illustrated that the modulation of the FeN₅ axial ligand resulted in less charge feedback from Fe to $-\text{SO}_4$ in a critical $[\text{FeN}_5\text{-SO}_4]$ transition state, enabling thermodynamically favorable electron capture from contaminants, and rapid regeneration of the site with low energy barriers for ultra-fast kinetic performance. Overall, this work provides a scientific basis for the preparation of biochar-based single-atom catalysts (SACs) with high metal-N coordination number (Metal-N_x, $x > 4$) for the efficient, low-cost, interference-resistant treatment of complex organic wastewater.

CRedit authorship contribution statement

Qing Du: Conceptualization, Data curation, Formal analysis, Investigation, Methodology, Software, Writing – original draft preparation. **Changqing Zhu:** Supervision, Methodology, Investigation, Software, Writing – review & editing. **Cailiang Yue:** Formal analysis, Supervision. **Fenxian Cun:** Writing- Review and Editing. **Zhilong Du:** Writing – review & editing. **Fuqiang Liu:** Resources, Supervision, Validation, Writing – review & editing, Project Administration, Funding Acquisition. **Aimin Li:** Resources, Supervision.

Declaration of Competing Interest

The authors declare that they have no known competing financial interests or personal relationships that could have appeared to influence the work reported in this paper.

Data Availability

Data will be made available on request.

Acknowledgments

This work was supported by the National Natural Science Foundation of China (No. 51522805, 51908273). This research used computational resources of the High-Performance Computing Center of Collaborative Innovation Center of Advanced Microstructures, Nanjing University.

Appendix A. Supporting information

Supplementary data associated with this article can be found in the online version at [doi:10.1016/j.apcatb.2023.123570](https://doi.org/10.1016/j.apcatb.2023.123570).

References

- [1] J. Xu, X. Zheng, Z. Feng, Z. Lu, Z. Zhang, W. Huang, Y. Li, D. Vuckovic, Y. Li, S. Dai, Organic wastewater treatment by a single-atom catalyst and electrolytically produced H_2O_2 , *Nat. Sustain.* 4 (2021) 233–241.
- [2] Y. Gao, T. Wu, C. Yang, C. Ma, Z. Zhao, Z. Wu, S. Cao, W. Geng, Y. Wang, Y. Yao, Activity trends and mechanisms in peroxymonosulfate-assisted catalytic production of singlet oxygen over atomic metal–N–C catalysts, *Angew. Chem. Int. Ed.* 60 (2021) 22513–22521.
- [3] A. Misra, C. Zambrozki, G. Kloker, A. Kotyba, M.H. Anjass, I. Franco Castillo, S. G. Mitchell, R. Güttel, C. Streb, Water purification and microplastics removal using magnetic polyoxometalate-supported ionic liquid phases (magPOM-SILPs), *Angew. Chem. Int. Ed.* 59 (2020) 1601–1605.
- [4] L. Chen, J. Duan, P. Du, W. Sun, B. Lai, W. Liu, Accurate identification of radicals by in-situ electron paramagnetic resonance in ultraviolet-based homogenous advanced oxidation processes, *Water Res.* 221 (2022), 118747.
- [5] Q. Zhong, C. Xu, Y. Liu, Q. Ji, Z. Xu, D. Sun, S. Zhou, B. Yang, Y. Dai, C. Qi, Defect-engineered $\text{FeSe}_2\text{-x@C}$ with porous architecture for enhanced peroxymonosulfate-based advanced oxidation processes, *Appl. Catal. B: Environ.* 309 (2022), 121259.
- [6] J. Song, N. Hou, X. Liu, M. Antonietti, P. Zhang, R. Ding, L. Song, Y. Wang, Y. Mu, Asymmetrically coordinated CoB_3N_3 moieties for selective generation of high-valent Co-oxo species via coupled electron-proton transfer in Fenton-like reactions, *Adv. Mater.* (2023), 2209552.
- [7] Y. Shang, X. Xu, B. Gao, S. Wang, X. Duan, Single-atom catalysis in advanced oxidation processes for environmental remediation, *Chem. Soc. Rev.* 50 (2021) 5281–5322.
- [8] Y. Wang, X. Duan, Y. Xie, H. Sun, S. Wang, Nanocarbon-based catalytic ozonation for aqueous oxidation: engineering defects for active sites and tunable reaction pathways, *ACS Catal.* 10 (2020) 13383–13414.
- [9] Y. Sun, J. Cao, Q. Li, D. Li, Z. Ao, Identifying key factors of peroxymonosulfate activation on single-atom M–N–C catalysts: a combined density functional theory and machine learning study, *J. Mater. Chem. A* 11 (2023) 16586–16594.
- [10] H. Xiang, W. Feng, Y. Chen, Single-atom catalysts in catalytic biomedicine, *Adv. Mater.* 32 (2020), 1905994.
- [11] X. Liang, D. Wang, Z. Zhao, T. Li, Y. Gao, C. Hu, Coordination number dependent catalytic activity of single-atom cobalt catalysts for fenton-like reaction, *Adv. Mater.* 32 (2022), 2203001.
- [12] H. Zhang, P. Cui, D. Xie, Y. Wang, P. Wang, G. Sheng, Axial N ligand-modulated ultrahigh activity and selectivity hyperoxide activation over single-atoms nanozymes, *Adv. Sci.* 10 (2023), 2205681.
- [13] Y. Zhang, J. Liu, J. Wang, Y. Zhao, D. Luo, A. Yu, X. Wang, Z. Chen, Engineering oversaturated Fe–N₅ multifunctional catalytic sites for durable lithium-sulfur batteries, *Angew. Chem. Int. Ed.* 133 (2021) 26826–26833.
- [14] H. Zhang, J. Li, S. Xi, Y. Du, X. Hai, J. Wang, H. Xu, G. Wu, J. Zhang, J. Lu, A graphene-supported single-atom FeN₅ catalytic site for efficient electrochemical CO_2 reduction, *Angew. Chem. Int. Ed.* 131 (2019) 15013–15018.
- [15] Z. Liu, H. Li, X. Gao, X. Guo, S. Wang, Y. Fang, G. Song, Rational highly dispersed ruthenium for reductive catalytic fractionation of lignocellulose, *Nat. Commun.* 13 (2022), 4716.
- [16] Y.N. Shang, X. Xu, B.Y. Gao, S.B. Wang, X.G. Duan, Single-atom catalysis in advanced oxidation processes for environmental remediation, *Chem. Soc. Rev.* 50 (2021) 5281–5322.
- [17] K. Yin, L. Peng, D. Chen, S. Liu, Y. Zhang, B. Gao, K. Fu, Y. Shang, X. Xu, High-loading of well dispersed single-atom catalysts derived from Fe-rich marine algae for boosting Fenton-like reaction: Role identification of iron center and catalytic mechanisms, *Appl. Catal. B: Environ.* 336 (2023), 122951.
- [18] D.P. Kumar, D. Ramesh, P. Subramanian, S. Karthikeyan, A. Surendrakumar, Activated carbon production from coconut leaflets through chemical activation: Process optimization using Taguchi approach, *Bioresour. Technol. Rep.* 19 (2022), 101155.
- [19] J. Liu, X. Kong, L. Zheng, X. Guo, X. Liu, J. Shui, Rare earth single-atom catalysts for nitrogen and carbon dioxide reduction, *ACS nano* 14 (2020) 1093–1101.
- [20] Y. Wang, H. Zhao, Y. Liu, J. Li, X. Nie, P. Huang, M. Xing, Environmentally relevant concentration of sulfamethoxazole-induced oxidative stress-cascaded damages in the intestine of grass carp and the therapeutic application of exogenous lycopene, *Environ. Pollut.* 274 (2021), 116597.
- [21] Y. Chen, B. Xi, M. Huang, L. Shi, S. Huang, N. Guo, D. Li, Z. Ju, S. Xiong, Defect-Selectivity and “Order-in-Disorder” Engineering in Carbon for Durable and Fast Potassium Storage, *Adv. Mater.* 34 (2022), 2108621.
- [22] Z. Xiong, Z. Huanhuan, W. Jing, C. Wei, C. Yingquan, X. Gao, Y. Haiping, C. Hanping, Physicochemical and adsorption properties of biochar from biomass-based pyrolytic polygeneration: effects of biomass species and temperature, *Biochar* 3 (2021) 657–670.
- [23] F. Wu, L. Chen, P. Hu, X. Zhou, H. Zhou, D. Wang, X. Lu, B. Mi, Comparison of properties, adsorption performance and mechanisms to Cd (II) on lignin-derived biochars under different pyrolysis temperatures by microwave heating, *Environ. Technol. Innov.* 25 (2022), 102196.
- [24] D. Zhong, Y. Jiang, Z. Zhao, L. Wang, J. Chen, S. Ren, Z. Liu, Y. Zhang, D.C. Tsang, J.C. Crittenden, pH dependence of arsenic oxidation by rice-husk-derived biochar: roles of redox-active moieties, *Environ. Sci. Technol.* 53 (2019) 9034–9044.
- [25] F. Yang, Q. Du, L. Sui, K. Cheng, One-step fabrication of artificial humic acid-functionalized colloid-like magnetic biochar for rapid heavy metal removal, *Bioresour. Technol.* 328 (2021), 124825.
- [26] X. Liang, D. Wang, Z. Zhao, T. Li, Z. Chen, Y. Gao, C. Hu, Engineering the low-coordinated single cobalt atom to boost persulfate activation for enhanced organic pollutant oxidation, *Angew. Chem. Int. Ed.* 303 (2022), 120877.

- [27] L. Jiao, G. Wan, R. Zhang, H. Zhou, S. Yu, H. Jiang, From metal-organic frameworks to single-atom Fe implanted N-doped porous carbons: efficient oxygen reduction in both alkaline and acidic media, *Angew. Chem. Int. Ed.* 57 (2018) 8525–8529.
- [28] H. Zhang, S. Hwang, M. Wang, Z. Feng, S. Karakalos, L. Luo, Z. Qiao, X. Xie, C. Wang, D. Su, Single atomic iron catalysts for oxygen reduction in acidic media: particle size control and thermal activation, *J. Am. Chem. Soc.* 139 (2017) 14143–14149.
- [29] Y.J. Sa, D.J. Seo, J. Woo, J.T. Lim, J.Y. Cheon, S.Y. Yang, J.M. Lee, D. Kang, T. J. Shin, H.S. Shin, A general approach to preferential formation of active Fe-Nx sites in Fe-N/C electrocatalysts for efficient oxygen reduction reaction, *J. Am. Chem. Soc.* 138 (2016) 15046–15056.
- [30] L. Jiao, R. Zhang, G. Wan, W. Yang, X. Wan, H. Zhou, J. Shui, S.H. Yu, H.L. Jiang, Nanocasting SiO₂ into metal-organic frameworks imparts dual protection to high-loading Fe single-atom electrocatalysts, *Nat. Commun.* 11 (1) (2020) 7.
- [31] L. Su, P. Wang, X. Ma, J. Wang, S. Zhan, Regulating local electron density of iron single sites by introducing nitrogen vacancies for efficient photo-fenton process, *Angew. Chem. Int. Ed.* 60 (2021) 21261–21266.
- [32] K. Qian, H. Chen, W. Li, Z. Ao, Y. Wu, X. Guan, Single-atom Fe catalyst outperforms its homogeneous counterpart for activating peroxymonosulfate to achieve effective degradation of organic contaminants, *Environ. Sci. Technol.* 55 (2021) 7034–7043.
- [33] X. Fu, X. Zhao, T.-B. Lu, M. Yuan, M. Wang, Graphdiyne-based single-atom catalysts with different coordination environments, *Angew. Chem. Int. Ed.* (2023).
- [34] C. Zhu, Y. Nie, F. Cun, Y. Wang, Z. Tian, F. Liu, Two-step pyrolysis to anchor ultrahigh-density single-atom FeN₅ sites on carbon nitride for efficient Fenton-like catalysis near 0 °C, *Appl. Catal. B: Environ.* 319 (2022), 121900.
- [35] J.J. Morgan, *Aquatic Chemistry-Chemical Equilibria and Rates in Natural Waters*, JOHN WILEY, USA, 1995.
- [36] M. Xu, H. Zhou, Z. Wu, N. Li, Z. Xiong, G. Yao, B. Lai, Efficient degradation of sulfamethoxazole by NiCo₂O₄ modified expanded graphite activated peroxymonosulfate: characterization, mechanism and degradation intermediates, *J. Hazard. Mater.* 399 (2020), 123103.
- [37] N. Li, R. Li, X. Duan, B. Yan, W. Liu, Z. Cheng, G. Chen, L. Hou, S. Wang, Correlation of active sites to generated reactive species and degradation routes of organics in peroxymonosulfate activation by co-loaded carbon, *Environ. Sci. Technol.* 55 (2021) 16163–16174.
- [38] **Environmental Quality Standards for Surface Water of China, GB 3838–2002.**
- [39] X. Yi, H. Ji, C. Wang, Y. Li, Y. Li, C. Zhao, A. Wang, H. Fu, P. Wang, X. Zhao, W. Liu, Photocatalysis-activated SR-AOP over PDINH/MIL-88A(Fe) composites for boosted chloroquine phosphate degradation: Performance, mechanism, pathway and DFT calculations, *Appl. Catal. B: Environ.* 293 (2021), 120229.
- [40] Z. Wang, Y. Liao, X. Li, C. Shuang, Y. Pan, Y. Li, A. Li, Effect of ammonia on acute toxicity and disinfection byproducts formation during chlorination of secondary wastewater effluents, *Sci. Total Environ.* 826 (2022), 153916.
- [41] G. Huang, C. Wang, C. Yang, P. Guo, H. Yu, Degradation of bisphenol A by peroxymonosulfate catalytically activated with Mn_{1.8}Fe_{1.2}O₄ nanospheres: synergism between Mn and Fe, *Environ. Sci. Technol.* 51 (2017) 12611–12618.
- [42] C. Zhu, F. Zhu, D.D. Dionysiou, D. Zhou, G. Fang, J. Gao, Contribution of alcohol radicals to contaminant degradation in quenching studies of persulfate activation process, *Water Res.* 139 (2018) 66–73.
- [43] E.T. Yun, J.H. Lee, J. Kim, H.D. Park, J. Lee, Identifying the nonradical mechanism in the peroxymonosulfate activation process: singlet oxygenation versus mediated electron transfer, *Environ. Sci. Technol.* 52 (2018) 7032–7042.
- [44] F. Liu, Y. Zhang, S. Wang, T. Gong, M. Hua, J. Qian, B. Pan, Metal-free biomass with abundant carbonyl groups as efficient catalyst for the activation of peroxymonosulfate and degradation of sulfamethoxazole, *Chem. Eng. J.* 430 (2022), 132767.
- [45] C. Zhu, Y. Nie, S. Zhao, Z. Fan, F. Liu, A. Li, Constructing surface micro-electric fields on hollow single-atom cobalt catalyst for ultrafast and anti-interference advanced oxidation, *Appl. Catal. B: Environ.* 305 (2022), 121057.
- [46] L. Wang, J. Jiang, S. Pang, Y. Zhou, J. Li, S. Sun, Y. Gao, C. Jiang, Oxidation of bisphenol A by nonradical activation of peroxymonosulfate in the presence of amorphous manganese dioxide, *Chem. Eng. J.* 352 (2018) 1004–1013.
- [47] R. Yuan, C. Yue, J. Qiu, F. Liu, A. Li, Highly efficient sunlight-driven reduction of Cr (VI) by TiO₂@ NH₂-MIL-88B (Fe) heterostructures under neutral conditions, *Appl. Catal. B: Environ.* 251 (2019) 229–239.
- [48] L. Zhang, X. Jiang, Z. Zhong, L. Tian, Q. Sun, Y. Cui, X. Lu, J. Zou, S. Luo, Carbon nitride supported high-loading Fe single-atom catalyst for activation of peroxymonosulfate to generate ¹O₂ with 100% selectivity, *Angew. Chem. Int. Ed.* 60 (2021) 21751–21755.
- [49] Y. Zhao, H. An, J. Feng, Y. Ren, J. Ma, Impact of crystal types of AgFeO₂ nanoparticles on the peroxymonosulfate activation in the water, *Environ. Sci. Technol.* 53 (2019) 4500–4510.
- [50] Z. Wang, W. Qiu, S.-Y. Pang, Q. Guo, C. Guan, J. Jiang, Aqueous Iron (IV)–Oxo complex: an emerging powerful reactive oxidant formed by iron (ii)-based advanced oxidation processes for oxidative water treatment, *Environ. Sci. Technol.* 56 (2022) 1492–1509.
- [51] N. Jiang, H. Xu, L. Wang, J. Jiang, T. Zhang, Nonradical oxidation of pollutants with single-atom-Fe (III)-activated persulfate: Fe (V) being the possible intermediate oxidant, *Environ. Sci. Technol.* 54 (2020) 14057–14065.
- [52] C.W. Chen, Y. Huang, Y. Hua, J. Qu, W. Xia, Dehua He, Chun Sharma, Virender K. Shu, Dong, Overlooked self-catalytic mechanism in phenolic moiety-mediated Fenton-like system: Formation of Fe (III) hydroperoxide complex and co-treatment of refractory pollutants, *Appl. Catal. B: Environ.* 321 (2023), 122062.
- [53] W. Ren, G. Nie, P. Zhou, H. Zhang, X. Duan, S. Wang, The intrinsic nature of persulfate activation and N-doping in carbocatalysis, *Environ. Sci. Technol.* 54 (2020) 6438–6447.
- [54] C. Zhu, S. Zhao, Z. Fan, H. Wu, F. Liu, Z. Chen, A. Li, Confinement of CoP nanoparticles in nitrogen-doped yolk-shell porous carbon polyhedron for ultrafast catalytic oxidation, *Adv. Mater.* 30 (2020), 2003947.
- [55] M. Zhang, C. Xiao, X. Yan, S. Chen, C. Wang, R. Luo, J. Qi, X. Sun, L. Wang, J. Li, Efficient removal of organic pollutants by metal-organic framework derived Co/C yolk-shell nanoreactors: Size-exclusion and confinement effect, *Environ. Sci. Technol.* 54 (2020) 10289–10300.